Fluctuations of the solid discharge of gravity-driven particle flows in a turbulent stream

Tobias Böhm
Cemagref, Domaine Universitaire BP 76, 38402 Saint-Martin-d'Hères Cedex, France

Christophe Ancey
Swiss Federal Institute of Technology, Ecublens, 1015 Lausanne, Switzerland

Phillipe Frey
Cemagref, Domaine Universitaire BP 76, 38402 Saint-Martin-d'Hères Cedex, France

Jean-Luc Reboud
University Joseph Fourier, LEMD, Grenoble, France

Christophe Ducottet
Laboratory TSI, UMR CNRS 5516, University of Saint Etienne, 42000 Saint Etienne, France
(Received 18 February 2004; published 23 June 2004)

Substantial variations in the particle flux are commonly observed in field measurements on gravel-bed rivers and in laboratory experiments mimicking river behavior on a smaller scale. These fluctuations can be explained by the natural variability of sediment supply and hydraulic conditions. We conducted laboratory experiments of particle transport down a two-dimensional inclined channel, for which the boundary conditions were properly controlled. Most flow variables and the features of particle trajectories were measured using a high-speed camera. The particles were 6-mm glass beads entrained by a rapid, turbulent, supercritical water flow. Even under these well-controlled experimental conditions and despite steady supply, solid discharge exhibited significant variations with time. The objective of this paper was to pinpoint the origins of these fluctuations by investigating different flow conditions. Two experiments were done with a fixed (smooth or corrugated) channel bottom and two others were run with a mobile bed (involving layers of closely packed particles lying along the channel base, which could be entrained by the stream); in the latter case, two particle arrangements were tested. It was found that, to a large extent, fluctuations reflected the finite size of the observation window. For fixed beds, the characteristic time scale of fluctuations and their probability distribution can be predetermined by evaluating the mean and fluctuating velocities of a single particle. Solid-discharge fluctuations were exacerbated when the bed was mobile because (i) the moving solid phase and the stationary bed exchanged particles and (ii) collective entrainment of particles occurred.

DOI: 10.1103/PhysRevE.69.061307 PACS number(s): 45.70.Mg, 45.50.−j, 47.85.−g, 92.10.Wa

I. INTRODUCTION

The objective of this paper is to examine the origins of solid-discharge fluctuations for flows of coarse particles driven both by gravity and drag exerted by a turbulent water stream. This issue comes up when studying the dynamics of particle transport from a microstructural viewpoint. Different forms of transport are produced depending on the particle weight and size relative to the turbulence scale. Light particles are maintained in suspension by turbulence whereas heavy particles roll along the bed or, when ejected from the bed, perform a series of leaps (saltation) [1]. Usually the Stokes number can be used to quantify the dependence of the two phases [2]. The Stokes number can be defined as follows: $\mathrm{St}=2/9(\rho_p/\rho_f)\mathrm{Re}_p$, where $\mathrm{Re}_p=Ud/\nu$ is the particle Reynolds number and ρ_p denotes particle density, ρ_f fluid density, $d=2a$ particle diameter, $U=|\overline{u_p}-\overline{u_f}|$ mean particle velocity $\overline{u_p}$ relative to the mean fluid phase velocity $\overline{u_f}$, and ν kinematic fluid viscosity. Here, typically, we investigate the case $\mathrm{St}=O(10^2)$. If the Stokes number is interpreted as the ratio of the particle relaxation time to a characteristic time of the fluid phase (here d/U), this means that there is a weak interplay between the two phases [3] and therefore the particle suspension flow must be treated as a two-phase flow at the macroscopic scale. A number of natural flows belong to this class; typical examples include sediment transport along gravel and sand-bed rivers (bed load transport), blowing sand, snow drift, etc.

Since it is difficult to analytically study the properties of two-phase flows, most models are based on substantial approximations of the interplay between the solid and fluid phases. In the field of bed load transport, the mean-field approximation primarily proposed by Bagnold [4] is a pervasive assumption. According to this hypothesis, the fluid shear stress at the bed τ_0 equals the threshold value τ_c corresponding to incipient motion of particles; the difference between the total bottom shear stress τ and τ_0 provides the shear stress in the solid phase. Interpreting the latter stress as the result of momentum transfers between the solid and fluid phases makes it possible to theoretically compute the number of particles that can be entrained and maintained in motion and, thereby, the solid flow rate (or solid discharge). Such an approximation leads to a solid discharge q_s in the form $q_s \propto (\tau-\tau_c)^{3/2}$. When compared with laboratory experimental

data or field measurements, this scaling correctly describes the sediment transport for steady uniform or gently varying flows [1]. However, for more general flow conditions, the Bagnold approximation yields poor results, notably for flows over arbitrarily sloping beds [5]. Furthermore, if bedforms (dune or antidune depending on the value of the Froude number) are interpreted as resulting from a loss of linear stability in the coupled fluid-solid system, the Bagnold assumption fails to capture the necessary physics since the resulting equations of motion do not show any instability [6].

The failure of the Bagnold assumption has renewed interest in a better understanding of the physical mechanisms of bed load transport. An alternative approach takes its roots in the work of Einstein [7]. In Einstein's view, a sediment transport does not result from an equilibrium in the momentum transfer between solid and liquid phases, but from the difference between the entrainment and deposition rates r_E and r_D, respectively, which are a function of the flow conditions and bed geometry. Stated more explicitly, this amounts to writing that on a small interval δx, the solid-discharge variation is $\delta q_s = (r_E - r_D)\,\delta x$. The solid discharge at bed equilibrium is the implicit solution to the equation $r_E = r_D$. Most theoretical models (e.g., see [8]) based on Einstein's approach are restricted to steady flows, for which such an equation can be solved, at least approximately. The full problem of determining how r_E and r_D are related to flow conditions remains unsolved. In addition to the complexity of the probabilistic formalism used by Einstein, this explains why such an approach has received little attention over the last 50 years.

Since our understanding of complicated particle systems and our ability to take accurate measurements on the particle scale have progressed a great deal since Einstein's time, it is now possible to more accurately examine the physics behind the entrainment and transport of coarse particles by turbulent flows. In preliminary investigations, we examined the motion of a single particle in a saltating [9] or in a rolling [10] regime from both experimental and theoretical perspectives. We then carried out new experiments with a continuous particle supply. Surprisingly enough, we observed substantial variations in the solid discharge with time, whereas the flow conditions were stationary on average: intermittent phases of transport and fluctuations as large as the mean solid discharge occurred. Such phenomena are frequent when fine particles are involved because their motion is controlled by fluid turbulence, but they were not expected here given the large size of particles used in our experiments. In order to gain insight into the origins of these fluctuations, we conducted further tests by varying the boundary conditions at the channel bottom: we used fixed channel bases (smooth or corrugated bottom) and mobile beds (the moving solid phase could exchange particles with the bed). Specific care was taken to distinguish between different artificial fluctuations and intrinsic fluctuations.

This paper attempts to understand why solid discharge exhibits large fluctuations in steady conditions. We shall see that the most plausible explanation lies in the collective motion of the particles entrained from the bed and that this collective motion is directly related to the particle arrangement inside the bed. We will begin by presenting the experimental facilities and procedures (Sec. II). Section III presents

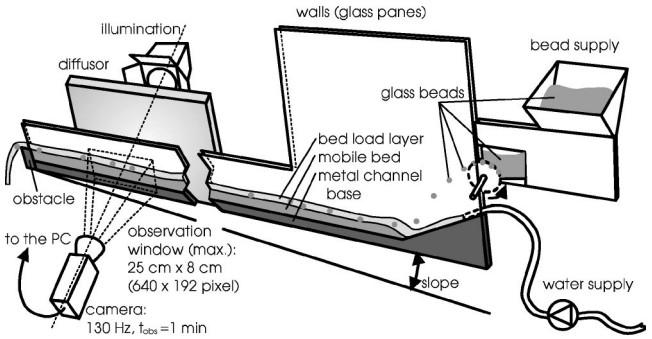

FIG. 1. Sketch of the experimental setup.

the experimental results for four different channel configurations. For all these configurations, the solid supply was kept constant at the channel inlet, but we modified the boundary conditions at the channel bottom by constraining particles to flow either over a fixed bed or an erodible bed.

II. EXPERIMENTAL FACILITIES AND TECHNIQUES

A. Channel

Experiments were carried out in a tilted, narrow, glass-sided channel, 2 m in length and 20 cm in height. Figure 1 shows a sketch of the experimental facility. The channel width W was adjusted to 6.5 mm, which was slightly larger than the particle diameter (6 mm). In this way, the particle motion was approximately two dimensional and stayed in the focal plane of the camera. The channel slope $\tan\theta$ was fixed at 10% for all the experiments presented in the present article.

Since the objective was to investigate the origins of solid discharge fluctuations, we ran experiments under different conditions:

(i) The first two experiments A and B were carried out with a fixed bed and thus were not intended to study erosion and sedimentation phenomena but to serve as a reference [see Figs. 2(a) and 2(b)]. We used two types of channel base: (i) a flat and smooth steel base, hereafter referred to as experiment A, and (ii) a corrugated bed made up of juxtaposed half cylinders (6 mm diameter), hereafter referred to as experiment B.

(ii) In experiments C and D, water flowed over a "mobile bed" made up of the same particles as those supplied at the channel entrance (see Sec. II B) allowing exchanges between the moving solid phase and the bed (erosion and deposition).

A bed is said to be mobile when it consists of particles that can be entrained by the stream. Mobile beds were obtained by building a disordered packing of particles along the channel bottom. Disorder was essential as it prevented slipping of entire layers of particles on the upper bed surface, which would have induced artificial erosion conditions. Maintaining disorder in monosized spherical particles is difficult, with severe constraints [11], here involving mainly how to create disorder in the packing and bed thickness. As regards the latter point, a random roughness made up of juxtaposed steel half-cylinders of radius r was positioned along the channel base. The arrangement of the particles constitut-

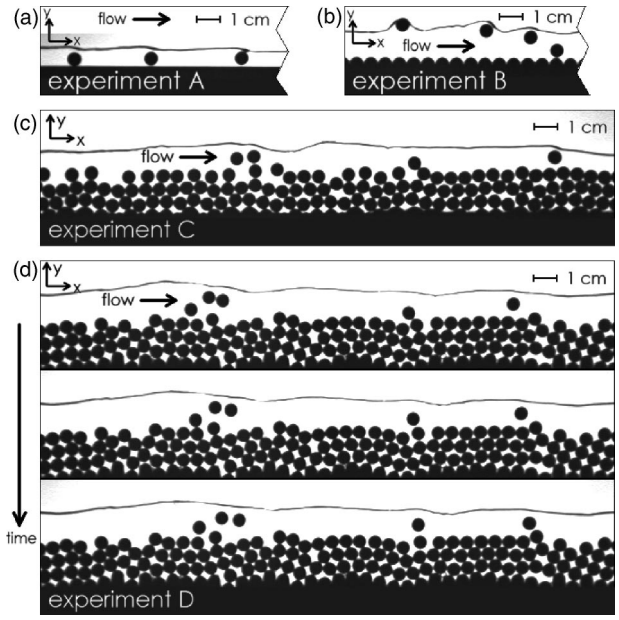

FIG. 2. Images of the particle transport for experiments A, B, C, and D. Image dimensions: 25 cm×5 cm (resolution: 640×120 pixels), (a) and (b) reduced; exposure time 0.2 ms, frame rate $f=129.2$ Hz, channel inclination $\tan\theta=0.1$. For experimental conditions, see Table I.

ing the bed depended a great deal on how the half-cylinders of the base were designed and disposed. We used two channel bases with different roughnesses:

(i) Channel base C consisted of half-cylinders of various sizes [see Fig. 2(c)]. We selected a mixture of three sizes of cylinders: their radius r could be either 1.5 mm, 3 mm, or 4 mm.

(ii) Channel base D consisted of half-cylinders of equal size ($r=3$ mm), but they were arranged on different levels, from 0 to 5.5 mm, by increments of 0.5 mm [see Fig. 2(d)]. These levels were generated using a sequence of uniformly distributed random numbers.

Selecting either of these roughnesses had a substantial influence on the short-range geometrical arrangement of the particles constituting the bed because the bed was thin. For thick beds (typically, whose thickness exceeded 5–6 particle diameters), a regular, crystalline arrangement was observed along the upper part of the bed. This is expected since it is well known that the disorder range induced by a defect in a crystalline arrangement of monosize spherical particles is a few particle diameters [11]. Therefore, in order to be able to control the order in the particle arrangement, we built beds whose thicknesses did not exceed 5 particle diameters.

Note that this bed thickness condition had severe consequences as regards the collisional interaction of a saltating particle with the bed. Indeed, in his experiments of dune formation, Rioual observed that the value of the effective coefficient of restitution depended on bed thickness [12]. This can be physically understood by recalling that the capacity of a particle to retrieve its momentum after impact depends on the reflection of the elastic waves generated during the collision. For a thick bed, considered as an infinite granular medium, the probability of an elastic wave to return to the impacting bead is very low, whereas for a shallow bed, a part of the elastic energy transferred during the collision can be restored to the bead.

TABLE I. Flow characteristics and time-averaged values of dimensionless numbers characterizing bed load and water flow. Constant parameters: channel inclination $\tan\theta=0.1$ and channel width $W=6.5$ mm.

Experiment	A	B	C	D
h(mm)	7.0	10.2	8.7	12.0
σ_h(mm)	0.7	1.5	1.9	2.2
$q_w(10^{-3}\ \mathrm{m^2/s})$	5.39	5.39	3.85	5.39
u_f(m/s)	0.77	0.53	0.44	0.45
$\dot{n}$(beads/s)	7.99	8.20	7.97	7.93
$\sigma_{\dot{n}}$(beads/s)	2.35	2.98	4.31	3.50
Re	6810	5200	4190	4590
Fr	2.98	1.73	1.68	1.40
ΔFr	0.464	0.377	0.544	0.385
N_{Sh}	0.078	0.114	0.096	0.133
Re_p	669	545	859	897
D	147	147	147	147
C_s	0.0258	0.0265	0.0360	0.0256
h/d	1.17	1.70	1.45	2.00

An obstacle was set at the channel outlet to enable bed formation and prevent full bed erosion; its height could be adjusted. The procedure used for building the bed is explained in Sec. II D.

B. Solid and water supplies

Colored spherical glass beads with a nominal diameter d of 6 mm and a density ρ_p of 2500 kg/m^3 (provided by Sigmund Lindner GmbH, Germany) were used. They were injected from a reservoir into the channel using a wheel driven by a direct current motor and equipped with 12 hollows on the circumference, as depicted in Fig. 1. For the experiments presented here, an injection rate of $\dot{n}_0=8$ beads per second was set, with an uncertainty of less than 5%. This corresponded to a solid discharge per unit width q_s of 1.39×10^{-4} m^2/s. The water supply at the channel entrance was controlled by an electromagnetic flow meter provided by Krohne (France). The discharge per unit width q_w ranged from 3 to 6×10^{-3} m^2/s.

C. Dimensionless numbers

The hydraulic conditions can be specified using classic dimensionless numbers. Table I reports the time-averaged values of these numbers. In Table I, σ_h and $\sigma_{\dot{n}}$ denote the standard deviations of the water depth and solid discharge, respectively. Here, to make the flow rate $\dot{n}$ more palpable, we express it in beads/s instead of m^3/s. The flow Reynolds number is defined as $\mathrm{Re}=4R_h\overline{u_f}/\nu$, where $R_h=Wh/(2h+W)$ denotes the hydraulic radius, $\overline{u_f}=q_w/h$ the fluid velocity (averaged in the y and z directions), ν the kinematic viscosity of

water, and h the water depth. The Froude number $N_{Fr} = \overline{u_f}/\sqrt{gh}$ (where g denotes gravity acceleration) varied significantly over the experiment duration and along the main stream direction. The mean N_{Fr} values and the variation scale Δ_{Fr} are reported in Table I. The variation scale of the Froude number was estimated assuming a constant water discharge and considering the variations in water depth: $\Delta_{Fr} = |\delta \mathrm{Fr}| = |3\mathrm{Fr}\ \sigma_h/2h|$. These numbers show that there were frequent transitions from subcritical to supercritical regimes for experiments C and D. This phenomenon seems intrinsic to bed load transport on a mobile bed (e.g., see [13]).

The Shields number is defined as the ratio of the bottom shear stress ($\tau_0 = \rho_p g h \tan\theta$) to the stress equivalent of the buoyant force of a particle lying on the bottom [1]: $N_{Sh} = \tau_0/[gd(\rho_p - \rho_f)]$. For our experiments, the critical Shields number $N_{Sh,c}$ corresponding to incipient motion is in the range 0.004–0.005 [9]. Here the reduced Shields number (also called the *transport stage*) $T_* = N_{Sh}/N_{Sh,c}$ is on the order of 25, which indicates that the flow regime is far above the threshold of motion. The particle Reynolds number can be defined as $\mathrm{Re}_p = |\overline{u_f} - \overline{u_p}|d/\nu$, where $\overline{u_p}$ denotes the mean velocity of a particle in motion. We furthermore introduced the dimensionless particle diameter $D = d\sqrt[3]{(\rho_p/\rho_f - 1)g/\nu^2}$ used in sedimentology to characterize the particle size compared to the turbulence scale [1]. The solid concentration is defined as the ratio of the solid and the water discharge $C_s = q_s/q_w$. Values reported in Table I are low, which indicates that particle flow was dilute. The ratio h/d is low, typically in the range 1–2.

Note that the dimensionless number values differ substantially from the values usually found in the sedimentology literature. The reason is twofold: first we used a short and narrow channel, which led to studying low-Reynolds-number regimes, whereas hydraulicians take care to avoid such regimes. Since we used coarse particles, particle motion was weakly dependent on the actual value of the flow Reynolds number and turbulence structure. Therefore we think that the small size of the experimental setup is not a handicap. Second we investigated supercritical flows because flow must be energetic enough to carry particles. However, in a supercritical regime, flow depth was low: on the order of the particle size, meaning that particle motion was affected by the water-free surface.

D. Experimental procedures

The procedure for experiments A and B was simple because the solid and water discharges could be chosen independently. In contrast, preparing experiments C and D was more complex. The preliminary procedure can be split into three major steps. First of all, a particle bed was build along the channel base, which remained stationary on average. To that end, an equilibrium between the water discharge, solid discharge, bed elevation, and channel slope was sought. This equilibrium was reached by using the following procedure.

(i) The water discharge q_w was set to a constant value.

(ii) An obstacle (approximately 20 mm in height) was positioned at the downstream end of the channel. The solid discharge $\dot{n}_0$ at the channel entrance (or the injection rate) was set to a constant value. The solid discharge per unit width q_s was calculated by the relation $q_s = \pi d^3 \dot{n}_0/(6W)$. An initial guess $\hat{q}_s$ for the solid discharge at equilibrium was obtained using an empirical sediment transport equation [14]. For our case (uniform sediment), this equation can be simplified into the form

$$\hat{q}_s = 6.27(q_w - q_c)\tan^2\theta, \tag{1}$$

where $q_c = 0.128\sqrt{g\,d^3}\tan^{-1.12}\theta$ is the critical o discharge corresponding to incipient motion of particles (here $q_c = 2.46\times10^{-3}\ \mathrm{m}^2/\mathrm{s}$). The first beads supplied by the feeding system were stopped by the obstacle at the channel outlet and started to form a bed. The bed line rose to the level of the obstacle and beads began to leave the channel. After approximately 10 min, the system arrived at bed load equilibrium; that is, there was no more bed deposition or erosion over a sufficiently long time interval.

(iii) In order to make the bed line parallel with the channel base, the water discharge was then adjusted. After several iterations, we arrived at the configuration of a bed that consisted of two to three almost stationary bead layers along the channel, for which the bed line slope matched the channel base inclination. Average equilibrium conditions were sustained over long time periods, basically as long as 30 min. The water discharge was set to $3.85\times10^{-3}\ \mathrm{m}^2/\mathrm{s}$ for bottom C versus $5.39\times10^{-3}\ \mathrm{m}^2/\mathrm{s}$ for bottom D: bed equilibrium was reached for significantly different water discharges (relative difference of 40%). This provided preliminary evidence of the substantial effect of particle arrangement on particle transport.

Once bed equilibrium was reached, the particles and the water stream were filmed using a Pulnix partial scan video camera (progressive scan TM-6705AN). The camera was placed perpendicular to the glass panes at a distance of 115 cm from the channel, approximately 80 cm upstream from the channel outlet. It was inclined at the same angle as the channel. Lights were positioned in the backside of the channel. An area of approximately 25 cm in length and 8 cm in height was filmed and later reduced to accelerate image processing.

The camera resolution was 640×192 pixels for a frame rate of $f = 129.2$ fps (exposure time: 0.2 ms, 256 gray levels). Each sequence was limited to 8000 images due to limited computer memory; this corresponded to an observation duration of approximately 1 minute. Figure 2 shows typical images for experiments A–D. Examining the short sequence of experiment D makes it possible to identify particles in a saltating or rolling motion.

E. Image processing

Images were analyzed using the WIMA software, provided by the Traitement du Signal et Instrumentation laboratory in Saint-Etienne (France). Positions of the bead mass centers were detected by means of an algorithm combining several image-processing operations. It compared the filmed images with the image of a model bead and calculated the correlation maxima to obtain the bead positions. The water-free

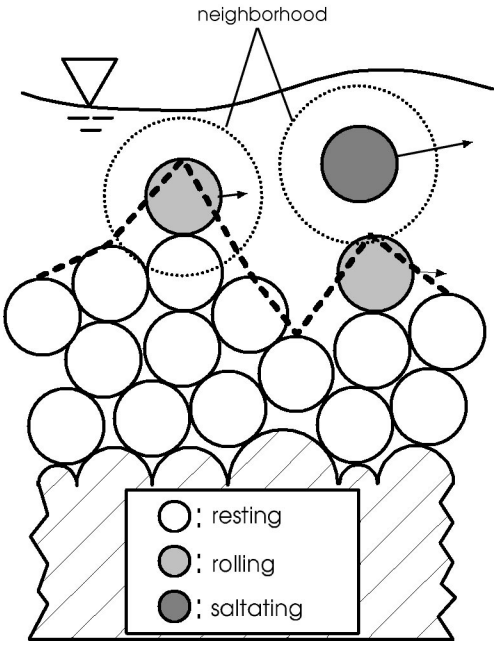

FIG. 3. Sketch defining the state of motion and the bed line.

surface (averaged in the direction perpendicular to the channel walls) was detected using its slim form; missing portions were interpolated or extrapolated. The resulting uncertainty in the bead and water line position was less than 1 pixel or 0.4 mm.

F. Data processing

Data obtained from the image sequences were analyzed to obtain the particle trajectories. For this purpose, we developed a particle-tracking algorithm, which was integrated into the WIMA software. This algorithm compared the bead positions of two consecutive images to determine the trajectory of each bead step by step. Since the particle movement was nearly two dimensional and the displacement of a particle between two images was always smaller than a particle diameter, the trajectories (approximately 700 per sequence) could be calculated with no significant error. Problems occurring at the entrance and exit of the observation zone prompted us to calculate variables such as the solid discharge in a reduced window 580 pixels in length.

Next the state of movement of a particle was defined by considering that each bead was always either in a resting, rolling, or saltating regime (see Fig. 3). Such partitioning posed several difficulties from the algorithmic viewpoint. The three states of movement were distinguished as follows.

(i) The resting beads formed the bed: they were in sustained contact with their neighbors. They were not expected to move or, more precisely, their possible drift velocities (together with fluctuating velocities) were lower than a threshold velocity u_t: $|\mathbf{u_p}| < u_t$, where $\mathbf{u_p}$ denotes the bead velocity averaged over five consecutive frames.

(ii) The beads in the rolling regime were located above the beads at rest: they remained in close contact with the bed and moved at a certain velocity. Our algorithm used two criteria to distinguish rolling beads: $|\mathbf{u_p}| \geqslant u_t$ (bead in motion) and $d_n/d \leqslant \varepsilon$ (particles in the vicinity), where d_n is the distance to the next neighbor (averaged over five consecutive frames) and ε is a threshold.

(iii) The beads in saltation leaped above the others. They had no close neighbors except when they collided with other beads. The algorithm distinguished saltating beads using the criteria $|\mathbf{u_p}| \geqslant u_t$ and $d_n/d > \varepsilon$.

The values of the threshold parameters u_t and ε were adjusted by trial and error to minimize the differences between the state determined by the algorithm and the state determined by the naked eye. Good agreement was obtained for $u_t = 0.025$ m/s and $\varepsilon = 1.07$.

For the experiments with a fixed bed (A and B), the water depth was directly computed by measuring the position of the water line with respect to the channel base. For the experiments with a mobile bed (C and D), the water depth was defined as the difference between the free surface and the bed surface elevation. This involved defining the bed surface. Arbitrarily, we considered that the bed surface profile is the dashed line linking the top points of the uppermost resting or rolling beads. Figure 3 depicts such a dashed line at a given time.

III. EXPERIMENTAL RESULTS

A. Overview

Since the primary objective was to understand the origins of the solid-discharge fluctuations, we paid particular attention to distinguishing between fluctuations intrinsic to the phenomenon and those coming from the measurement system (finite size of the observation of the window, acquisition rate, etc.). The solid discharge Q_s is usually defined as the flux of particles through a flow cross section $\mathcal{S}$: $Q_s = \int_S d\mathcal{S}\mathbf{u}_p \cdot \mathbf{k}$, where $\mathbf{k}$ is the unit normal to $\mathcal{S}$. This definition, suitable to continuum fields, is not well suited to discrete elements. A more convenient definition is to introduce the flow rate in terms of the probability $P[\mathbf{u}_p|\mathbf{x},t]$ that a particle crosses the control surface S at position $\mathbf{x}$ and time t with velocity $\mathbf{u}_p$:

$$Q_s = \int_S \int_{\mathbb{R}^2} |d\mathbf{x}| d\mathbf{u}_p P[\mathbf{u}_p|\mathbf{x},t] \mathbf{u}_p \cdot \mathbf{k}. \tag{2}$$

Under steady conditions ($\partial P/\partial t = 0$), this definition can be worked out as

$$Q_s = \lim_{V\to\infty} \frac{1}{V} \sum_{i=1}^{N} u_i v \mathcal{S} = \lim_{L\to\infty} \frac{v}{L} \sum_{i=1}^{N} u_i, \tag{3}$$

in which the ensemble average has been replaced by a volume average. The integration has been made on a control volume $\mathcal{V} = \mathcal{S} \times L$ of length L and volume $\mathcal{V}$. We have also used $v = 4\pi a^3/3$, the particle volume; $u_i = \mathbf{u}_p \cdot \mathbf{k}$, the streamwise velocity component of particle i; and N, the number of particles in motion in the control volume. Therefore, in the following, we shall define the flow rate $\dot{n} = Q_s/v$ as

$$\dot{n} = \frac{1}{L}\sum_{i=1}^{N} u_i. \tag{4}$$

An ideal experimental setup would be based on (i) an observation window with a length L that outweighs the mean distance λ between two moving particles and (ii) an acquisition rate much larger than the inverse of the typical particle time scale, computed as the time needed for the particle to move across the window.

In our laboratory experiments, the typical acquisition rate f, particle velocity u_p, and window length L were approximately 130 Hz, 0.3 m/s, and 25 cm, respectively. The supply rate of particles being $\dot{n}_0 = 8$ beads/s, we deduce that the interparticle length scale is on the order of $\lambda = u_p/8 \approx 38$ mm and the mean time for a particle to move across the window is on the order of $t_c = L/u_p = 0.8$ s. These estimates lead to the ratio $L/\lambda \approx 7$ and $f/(1/t_c) = 104$, which means that condition (ii) above is met whereas condition (i) is not. Resulting from the finite size of the observation window and the channel, artificial fluctuations were generated in the time records of solid discharge. Another source of fluctuations comes from the solid supply system. The bead supply system was designed to ensure a constant injection rate. However, we observed slight variations in the bead position and velocity at the moment of the release from the transport wheel. The beads thus impacted on different points of the channel, which led to nonuniform distances between two consecutive beads. For the experiments with a fixed bed (A and B), this deficiency was reflected by a strong variation in the number of beads in the window. In contrast, for the mobile bed experiments, we expected that the influence of the supply system on the flow in the observation window was weak because of the buffer effect of the bed: since the observation window was located 1.2 m from the channel inlet, an injected bead was likely to experience several jumps and/or transitions to rest before reaching the observation window; it is thus unlikely that this bead kept memory of its initial conditions.

The time records of the solid discharge were analyzed by taking a closer look at its empirical probability distribution and its correlation function. In addition, we carefully examined the features of the particle trajectories such as the types of motion as well as the leap length and height of saltating particles. To synthesize this information, we reported the particle movements in a space-time diagram. We further studied the structure of the bed arrangement. The main results are reported in Fig. 4 (flow-rate variation with time), Fig. 5 (autocorrelation of $\dot{n}$), and in Fig. 6 (probability distribution of $\dot{n}$); they are analyzed in the following sections.

B. Smooth bottom (experiment A)

The simplest configuration is a water stream over a flat surface. In this case, it is expected that particles roll or slide quickly as a result of the driving force exerted by gravity and water drag. Assuming that a test particle reaches a steady regime, we can express the momentum equation as a balance between the streamwise component of gravity acceleration $m'g \sin\theta$ and the mean water drag force $C_D \rho_f \pi a^2 |u_p - u_f|^2/2$. We used the following notation: $m' = 4\pi a^3(\rho_p - \rho_f)/3$ is the buoyant particle mass and C_D the drag coefficient; typically for high particle Reynolds numbers and confined flows, the drag coefficient is close to unity [10]. The mean particle velocity is then

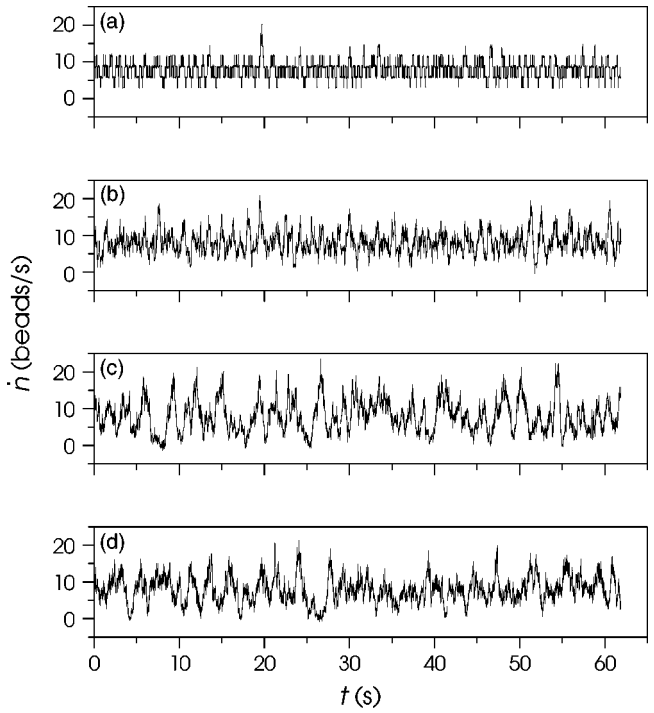

FIG. 4. Variation in the measured solid discharge with time for experiments A–D.

$$\overline{u_p} = \overline{u_f} - \sqrt{\frac{8}{3}\frac{\rho_p - \rho_f}{\rho_f}\frac{\sin\theta}{C_D} ag}.$$

As shown in Table I, the mean fluid velocity was 0.77 m/s and particle velocity should have been close to 0.61 m/s. The interparticle distance was then $\lambda = \frac{1}{8}\,0.61 \approx 7.7$ cm and thus, in the observation window (580 pixels or equivalently $L = 22.5$ cm), we must count 2.94 particles on average or, to be more specific, 6% of the recorded frames should include two particles and 94% should contain three particles. As a

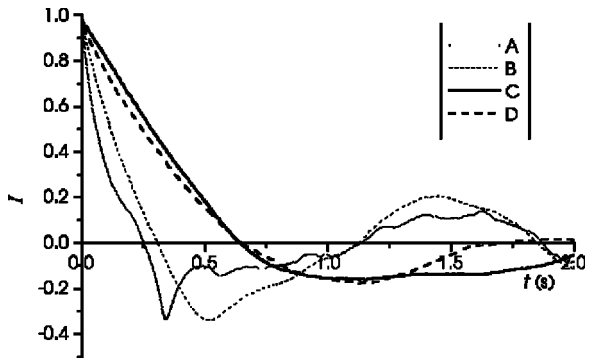

FIG. 5. Autocorrelation functions for experiments A–D.

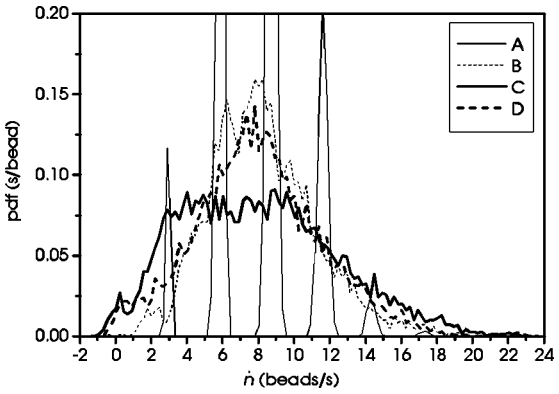

FIG. 6. Empirical probability density functions for experiments A–D.

result, the solid discharge should oscillate with two possible states: $\dot{n}=5.45$ beads/s and $\dot{n}=8.17$ beads/s.

Time variations in $\dot{n}$ are plotted in Fig. 4(a). The autocorrelation of the signal are reported in Fig. 5. The time variations in solid discharge were step shaped, which means that the solid-discharge function was valued over a finite set of possible values and thus $\dot{n}$ behaved as a discrete random variable. This is probably best seen in the probability density function (pdf) plot: Figure 7 shows the scaled histogram of the recorded values and the expected probability distribution deduced using heuristic arguments. As expected, two peaks are found in the $\dot{n}$ pdf, but marginal spikes are also present. As shown in the inset of Fig. 7, although there is not much difference between the measured and expected average number of particles contained in the observation window (2.66 against 2.94), the probability density function of the particle number was much wider than expected: on rare occasions, up to seven particles could be observed in the window. This difference between the expected and observed values mainly resulted from small irregularities in bead supply at the channel inlet.

Another striking result is that there was not much difference between the probability distributions of N and $\dot{n}$ in

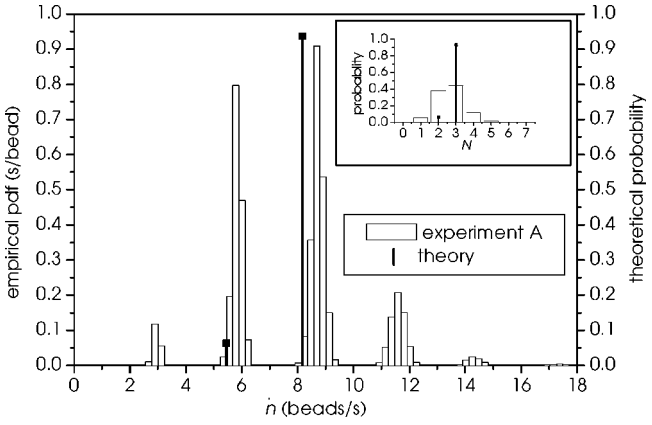

FIG. 7. Probability density function (pdf) of the solid discharge $\dot{n}$. The white histogram gives the empirical pdf of the observed values while the bold lines (here two peaks) stand for the theoretical mass distribution of $\dot{n}$. In the panel, the probability distribution of the number N of particles counted in the observation window is reported.

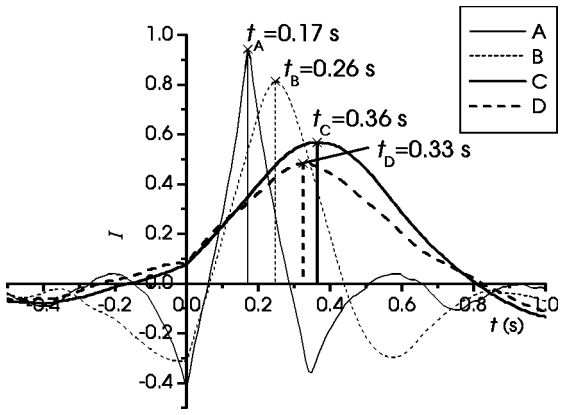

FIG. 8. The normalized intercorrelation functions of the solid discharge $\dot{n}$ computed over either half window for experiments A–D.

terms of their shape, demonstrating that the particle velocity was fairly constant and close to the mean value. Experimentally, we found that the mean value of $\overline{u_p}$ was 0.65 m/s, while our heuristical approach gives an estimate of 0.61 m/s, in fairly good agreement with the observed value.

Figure 8 reports the intercorrelation function of the solid discharge. It was obtained by dividing the observing window vertically into two halves and calculating the time evolution of the solid discharge for either half [see Eq. (4)]. The intercorrelation function was computed by taking normalized signals $[\dot{n}(t)-\overline{\dot{n}}]/\sigma_{\dot{n}}$.

For experiment A, this yields a spike function with a maximum at the characteristic time of $t_A=0.17$ s. This time is consistent with the travel time of a particle: since the average velocity was 0.65 m/s, the time required for a particle to cross half the window was $t=0.174$ s. The high value reached by the maximum shows that the signal changed only slightly between the two window halves because the interparticle distances once established at the channel inlet did not change along the channel. The channel base did not introduce any significant perturbation to the particle movement.

In short, we have found that, for smooth beds, the observed fluctuations in solid discharge essentially came from the finite size of the observation window compared to the particle diameter. In such experiments, solid-discharge fluctuations induced by water turbulence were low.

C. Corrugated bottom (experiment B)

In order to test the influence of the bottom roughness, we conducted a further experiment replacing the smooth base by a corrugated surface. A wider range of the particle velocity was expected as a result of collisions with the corrugated bottom. This should generate larger fluctuations in the solid discharge than in the previous case. To compute the probability density function of the flow rate, we used the following assumptions: (1) the number of particles included in the observation window is distributed according to a Poisson distribution, (2) the streamwise components of particle velocity is Maxwellian, and (3) the particle velocity distribution is

independent of the particle number (because flow is dilute). Under these assumptions, it can be shown (see the Appendix) that

$$P_{\dot{n}}(\dot{n}|L) = \sum_{k=1}^{\infty} \frac{e^{-\mu}\mu^k}{k!\sqrt{2\pi k}} \frac{L}{\sigma_u} \exp\left[-\frac{(L\dot{n} - k\overline{u})^2}{2k\sigma_u^2}\right],$$

where σ_u^2 is the particle velocity variance (streamwise component), $\overline{u}$ its average, and μ is the average number of particles moving in the observation window. No closed analytical expression was found, but numerical estimations can easily be made because of the rapid convergence of the sum and the moments of $P_{\dot{n}}$ can be analytically determined (see the Appendix). Notably it is shown that the average flow rate is $\mu\overline{u}/L$, as expected, and its variance is $\mu\sigma_u^2/L^2$. As previously, the mean number of particles contained in the observation window can be estimated from the mean interparticle distance λ imposed by the particle supply frequency ω_0 (here $\omega_0 = 8$ Hz) and particle velocity: $\mu = L/\lambda$ with $\lambda = \omega_0^{-1}\overline{u_p}$. Therefore, we find that the mean flow rate equals the supplied flow rate $\dot{n}_0$ and its variance is

$$\mathrm{Var}[P_{\dot{n}}] = \frac{1}{L}\frac{\sigma_u^2}{\overline{u_p}}. \tag{5}$$

From a theoretical viewpoint, solid discharge fluctuations result from the finite size of the channel (factor L^{-1}) and velocity fluctuations of individual particles (factor $\sigma_u^2/\overline{u_p}$). Note that if we replace the values of L, σ_u, and $\overline{u_p}$ by the measured values, we find that the variance of $\dot{n}_0$ is substantially affected by L.

Experimentally, the water discharge was unchanged compared to run A, but the water level rose considerably due to the higher dissipation rate at the bottom (see Table I). The injection rate being unchanged, the beads were mostly in saltation; rolling motion occurred marginally (it contributed to the solid discharge at less than 1.5%). We counted 2321 leaps, with a mean length and height of 6.5 and 1.2 particle diameters, respectively. The values of the dimensionless leap length and height for our experiment B are nevertheless consistent with the work of Niño *et al.* [15], despite the substantial differences in the two experimental configurations. Because of the variability induced by the collisions with the channel bottom, the particle velocity varied within a wider range: the average value $\overline{u_p}$ and the standard derivation σ_u were 0.44 m/s and 0.10 m/s, respectively. The number of particles in the window (see Fig. 9) ranged from 0 to 10 (versus 0 to 7 for the smooth base). As a consequence, the pdf plot of the solid discharge was continuous and bell shaped at first sight. A closer look reveals that there were several local maxima in the histogram but they were less pronounced than those observed in experiment A. As shown in Fig. 10, the empirical distribution is in fairly good agreement with the theoretical expression: the local peak positions and the tail behavior are reasonably described by the theoretical predictions.

The autocorrelation of the signal has been reported in Fig. 5. Note that there are slight differences between the autocorrelation functions pertaining to experiments A and B. Easier to interpret is the intercorrelation function. Here the intercorrelation function of the solid discharges was computed in either window half. The resulting function has been plotted in Fig. 8. For experiment B, the correlation maximum was situated at $t_B = 0.25$ s. This characteristic time is consistent with the mean time a bead takes to travel half of the window: $t = L/(2\,\overline{u_p}) = 0.26$ s. Compared to experiment A, the peak of the function was slightly less acute and spread out more widely. This shows that particle flow was not only advected with mean velocity $\overline{u_p}$, but there was also a diffusive process induced by particle velocity fluctuations.

In short, experimental results provide evidence that solid-discharge fluctuations come from both finite-size effects of the observation window and, to a lesser extent, particle velocity fluctuations.

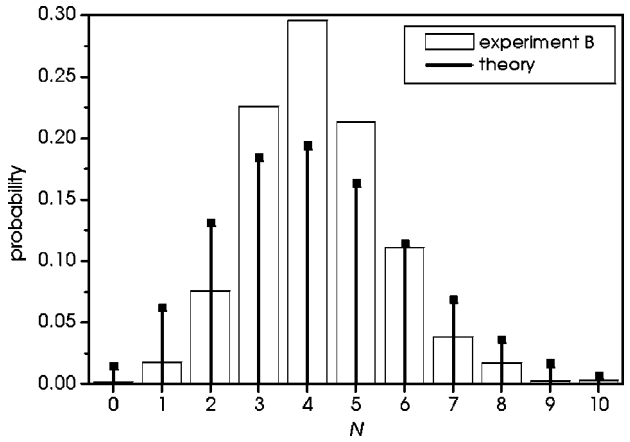

FIG. 9. Probability distributions of the number N of particles counted in the observation window. The white histogram represents experiment B and the black lines a theoretical distribution (Poisson distribution).

D. Ordered mobile bed (experiment C)

The next step was to study the interaction between the particles and a mobile bed (see Sec. II A). Compared to ex-

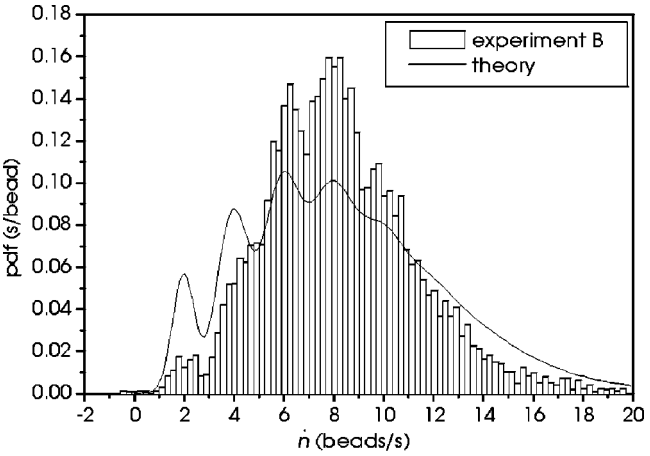

FIG. 10. Probability density functions (pdf) of the solid discharge $\dot{n}$. The white histogram and the black line represent the empirical and the theoretical pdf, respectively.

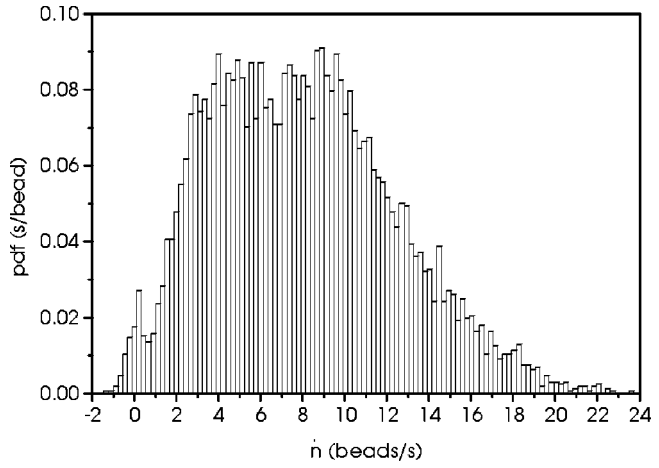

FIG. 11. Probability density function (pdf) of the solid discharge $\dot{n}$ for experiment C.

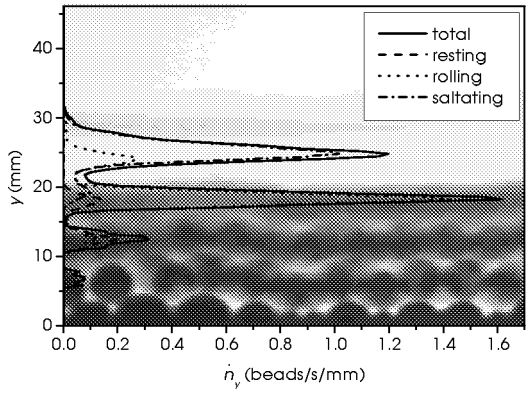

FIG. 12. The solid discharge $\dot{n}$ in function of the y coordinate, divided into the fractions of the state of movement, for experiment C. In the background the cumulated image of the sequence are plotted.

periments A and B, the chief difference is that the moving solid phase can exchange particles with the mobile bed. The assumptions used in the heuristic model described in Sec. II C are no longer valid, notably because the particle velocity fluctuations cannot be described by a Maxwellian distribution, since particles experienced different types of motion (rolling, saltating, entrainment-deposition). A problem in interpreting experiment C results (and afterwards experiment D) is that, as far as we know, there is currently no microstructural theoretical work on the particle exchanges between a mobile bed and a turbulent stream transporting coarse particles. Compared to simple experimental configurations A and B, it is more difficult to distinguish between artificial and intrinsic fluctuations of solid discharge. This led us to thoroughly examine the flow features by relating the solid discharge to particle trajectories.

Experimentally, because of the interplay between solid and fluid phases, solid and water discharges could no longer be set independently. In order to enforce bed load equilibrium, the water discharge was set to a considerably lower value for experiment C than for the other experiments. However, the water level was only slightly lower than in experiment B (see Table I), as a result of energy dissipation induced by particle collisions. Beads were observed in the saltating, the rolling, and the resting regimes. This is why the number of leaps counted (1437) was lower than for experiment B. The mean leap length and height reduced to 3.7 and 0.37 particle diameters, respectively, which is significantly lower than values found by other authors because the trajectories of saltating particles were extremely constrained by the water-free surface and the mobile bed.

Figure 11 shows a fairly compact probability distribution for the flow rate $\dot{n}$. The small spike at approximately 0 indicates that there were phases without bed load transport. The distribution showed a large plateau between the values of $\dot{n} \approx 3$ beads/s and $\dot{n} \approx 11$ beads/s, as though the flow rate was uniformly distributed within this range.

The autocorrelation of the solid discharge has been reported in Fig. 5. Compared to experiments A and B, the time correlation was increased. This enhanced memory effect can result from (i) the increased number of particles in the observation window and (ii) decreased mean particle velocities for experiment C compared to runs A and B. Note that there was not much difference between experiments C and D, despite their significant differences as regards the solid-discharge probability distribution. We have also computed the intercorrelation function (see Fig. 8). The characteristic time of the intercorrelation function $t_C = 0.36$ s was longer than for the previous experiments. We measured a mean velocity for the beads in the rolling regime ($u_r = 0.062$ m/s) and another one for the beads in saltation ($u_s = 0.30$ m/s). Only the latter yields a travel time $[t = L/(2u_s) = 0.38$ s] that was consistent with the time given by the intercorrelation function. The peak was wider and lower than that observed for the previous experiments, which reveals a substantial diffusion of the flow rate in the streamwise direction. In this experiment, intermittent motion was frequent: a number of beads experienced different rolling and resting regimes. These beads needed much more time than the characteristic time t_C to travel half of the window, which contributed to increasing the tail of the intercorrelation function.

In order to gain insight into the properties of $\dot{n}$, we examined how the flow rate $\dot{n}$ was distributed in the vertical direction. The background of Fig. 12 was obtained by superimposing all the images of the filmed sequence. In the lower part of the figure, beads can be clearly distinguished because they did not move during the sequence. Above this stationary bed, intermittent movements of beads can be observed. Far from the stationary layers, the image becomes blurred and lighter because fast-moving beads left only fuzzy traces. In experiment C, the layer structure of the bed is obvious. This can also be seen in the curve of the time-averaged solid discharge as a function of the flow depth reported in the same figure. In addition, we plotted the individual contribution of saltating, rolling, and resting phases to the total discharge. The diagram reveals a splitting of the solid discharge into three fractions across the y axis. The small peaks at $y = 6$ mm and 12 mm mainly represent transport at very low velocities—i.e., beads in the resting regime. The peak at $y = 18$ mm reflects the predominance of the rolling regime, whereas the peak at $y = 25$ mm represents the saltating fraction. The distance between two peaks corresponds to the par-

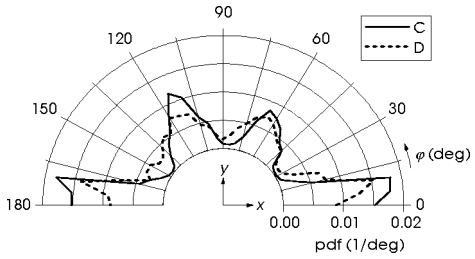

FIG. 13. The pdf of the contact angle φ between the beads in rest. Experiments C and D.

ticle diameter d. The formation of sharp peaks in the diagram provides evidence that the structure of horizontal bead layers in experiment C influenced a great deal the transport. The solid discharge can thus be decomposed mainly into the saltating regime (41.4%) and the rolling regime (46.6%); the contribution of the beads at rest (moving at low drift velocities) was low (10.0%).

These solid-discharge properties depend to some extent on the particle arrangement of the bed. To study the structure of the two-dimensional bed more precisely, we calculated the packing fraction C_p of the beads at rest. For this purpose, we calculated the border polygon in the (x,y) plane that included all the centers of the beads at rest. The packing fraction was defined as the ratio between the part of the surface occupied by beads to the total surface of the polygon. The time-averaged value was $C_p=0.846$, which lay midway between the values of a square lattice ($C_p=0.785$) and a triangular lattice, the densest packing ($C_p=0.906$). The packing fraction parameter was not sufficient to describe the bed structure given that it differed only slightly between experiments C and D (see also Sec. III E). We therefore examined the local order of the arrangement considering neighboring particles. This leads to introducing the contact angle: The contact angle φ is defined as the angle between the x direction and the line linking the centers of mass of two beads in sustained contact. Figure 13 plots the time-averaged probability density function of contact angles for all the beads constituting the bed (solid line for experiment C). A polar plot was used for an easier comparison with the images of Fig. 2; a bin size of 5° was chosen. Only the range 0–180° of the function is shown. It can be seen that contacts were found most frequently in the horizontal direction. This heterogeneity in the contact angle distribution results from the statistical computation being made on a collection of beads, which spanned nearly 40 particle diameters in the x direction, but only approximately 3 in the y direction. There is a second maximum near 120° and a third one at 60°, revealing that the bed structure was not too far from a crystalline structure (triangular lattice). Contacts in the 120° direction were more frequent than those in the 60° direction. This indicates that beads in the upper part of the bed frequently came to a halt against a bead in the downstream direction, at an angle of 120°. There were almost no contacts between these peaks.

Since the bed was permanently rearranged as a result of interactions with moving particles, it tended to build up regular structures. The disorder imposed by the channel base was not sufficient to prevent formation of horizontal layers. The order in the bed implied an intermittent movement of fairly long series of particles. The fluctuations of the solid discharge were, to some extent, influenced by the bed arrangement.

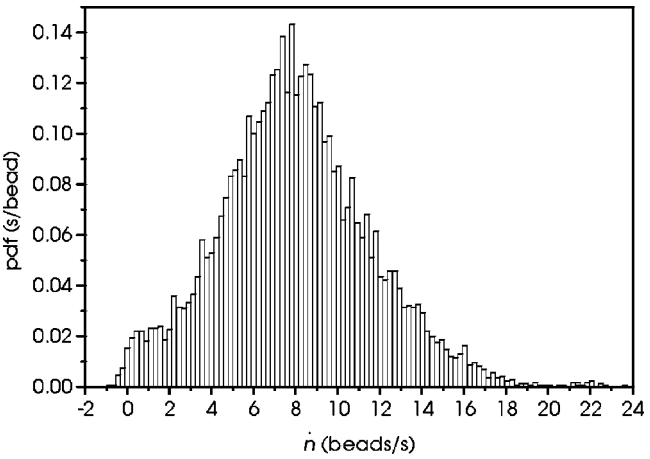

FIG. 14. Probability density function (pdf) of the solid discharge $\dot{n}$ for experiment D.

E. Disordered mobile bed (experiment D)

Our intention was to reduce artificial ordering effects of a two-dimensional particle arrangement as much as possible. To limit the formation of horizontal bead layers, we constructed another channel base [see Fig. 2(D)]. Similarly to experiment C, beads were observed in a saltating-rolling regime. However, the bead arrangement of the bed changed the characteristics of the transport considerably. We counted 1461 leaps with a mean length and height of 4.4 and 0.50 particle diameters, respectively. The augmentation with respect to experiment C was due to the increase in the water depth. The water discharge when bed load equilibrium conditions were achieved was considerably higher than for experiment C; the water depth value was thus higher as well. The pdf plot of the solid discharge was bell shaped and nearly symmetric (see Fig. 14). There was, however, an accumulation of phases with low transport rates ($\dot{n} \approx 1$ bead/s).

The characteristic time of the intercorrelation function was $t_D=0.33$ s (see Fig. 8) and differed only slightly from that of experiment C. The mean velocity of the saltating beads ($u_s=0.30$ m/s) was very close to the velocity found for experiment C. As previously, the characteristic time can be directly related to this saltating particle velocity, but not the rolling particle velocity ($u_r=0.062$ m/s).

As for experiment C, we calculated the time-averaged solid discharge as a function of the y coordinate (see Fig. 15). Here, rolling and saltating phases appeared in wider, overlapping zones. Both saltation and rolling zones showed a peak at $y=26$ mm; the rolling zone had an additional peak at $y=19$ mm. While the peaks were less pronounced than for experiment C, the distance between them still corresponded to d. The solid discharge could be broken down into three contributions: 56.9% of $\dot{n}$ resulted from saltating particles,

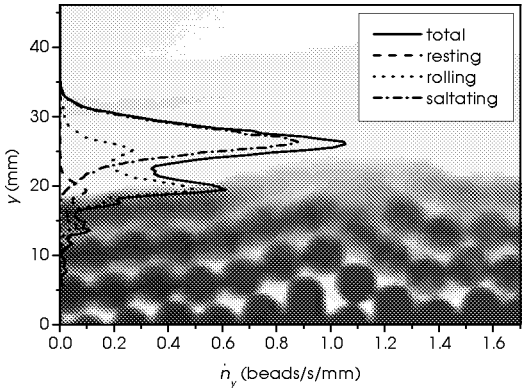

FIG. 15. The solid discharge $\dot{n}$ as a function of the y coordinate (total solid discharge and elementary contributions) for experiment D. In the background the cumulated images of the sequence are plotted.

36.1% from rolling beads, and 7.0% from creeping beads of the bed (versus 41.4%, 46.6%, and 10.0%, respectively, for experiment C). Compared to experiment C, the rolling movement was less frequent. This can be shown by looking at the superimposed images of the sequence in the background of Fig. 15: there was more disorder in the bead arrangement, which prevented long layers of beads from sliding. In other words, to reach the imposed total solid discharge, the water stream was more intense than for experiment C (flow rate 40% higher than for experiment C) and therefore could transport more saltating particles. This reveals the tremendous interplay between the water flow rate, the bed arrangement, and the moving solid phase: small changes in the bed configuration led to substantial variations in the water flow rate and solid phase features.

The changes in the bed configuration mainly resulted from the particle arrangement. Indeed, the packing fraction of the resting beads $C_p=0.827$ was only slightly lower than the value obtained for experiment C. Differences in the bed arrangement could be seen in the pdf of the contact angles shown in Fig. 13 (dashed line for experiment D), which was more evenly distributed than for experiment C. The maxima were lower and the minima less pronounced. However, the crystalline symmetry was not completely broken.

To relate solid-discharge fluctuations to particle trajectories, it is interesting to examine the spatiotemporal bead propagation by reporting the particle movement in the (x,t) plane. Figure 16 shows the bead propagation, including a sketch of how the diagram was obtained. Only beads in saltation (black lines) and rolling (gray lines) are presented; beads at rest have been omitted for the sake of clarity. Beads entered the observation window on the left and left it on the right. The time propagation is downwards. Since the x component of the velocity of a bead is the ratio between the x displacement and the elapsed time, it is equivalent to the slope of the trace. Given that beads usually moved faster in the saltating regime than in the rolling regime, the $\Delta x/\Delta t$ quotient was larger, which can be seen in the diagram. Note as well that the beads in saltation typically traveled distances as long as the window length before coming to rest, whereas beads in the rolling regime often moved only a few bead diameters before stopping again.

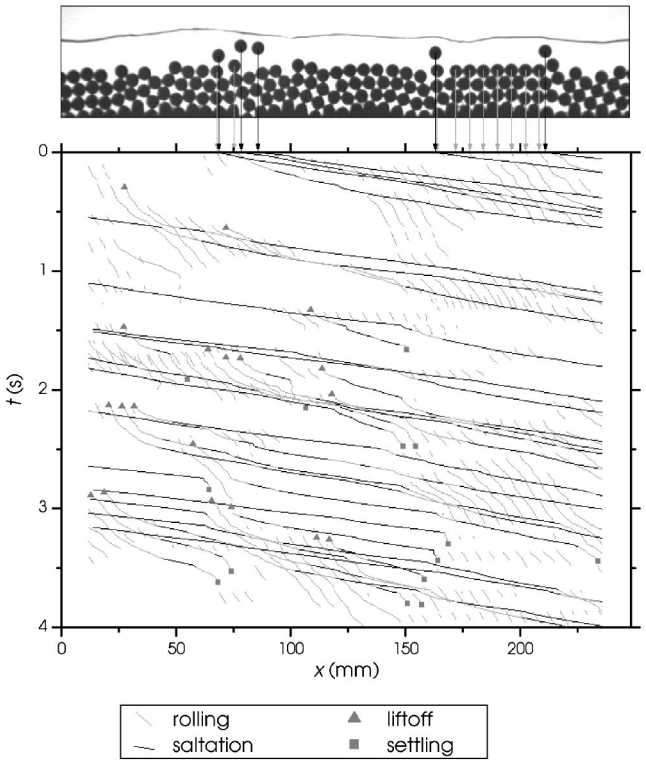

FIG. 16. From the image sequence to the bead propagation in the plane (x,t). Experiment D.

Furthermore, different events (at a certain x position and a certain time; see Fig. 16) could be observed, for example:

(i) A bead in saltation overtook another one in the rolling regime and the traces intersected (see Fig. 16 at $x\approx 80$ mm, $t\approx 0.1$ s).

(ii) A series of four particles was set into rolling movement (see Fig. 16 at $x\approx 150$ mm, $t\approx 0.4$ s).

(iii) A bead in saltation was decelerated suddenly because of a collision with another bead. It switched into a rolling regime but returned to saltation a few images later. The bead that had been hit moved about one diameter then came back to rest (see Fig. 16 at $x\approx 150$ mm, $t\approx 1.5$ s).

Note that, in the diagram of Fig. 16, we show only 4 s of the sequence, whose total duration exceeded 60 s. The cited events were nevertheless typical of the experiment and reproduced with modifications over the whole sequence.

The diagram shows that there were beads frequently switching between rest and rolling; others were switching between the rolling and saltating regimes, whereas the transition from rest to saltation via rolling (or from saltation to rest) was rare. We studied these cases of a bead liftoff and settling more precisely. This first required defining the regime transitions more accurately. A bead that stayed at least five images (0.039 s) at rest and then (at least) five images in saltation (with a rolling phase of arbitrary duration in between) was defined as liftoff; settling was defined in the same way. In the diagram of Fig. 16, we marked the transition from rest to rolling (from rolling to rest) of the liftoff events (the settling events) by triangles (squares). A striking feature is that the liftoff and settling events often occurred in tight ranges of x. We observed, for example, seven liftoffs in

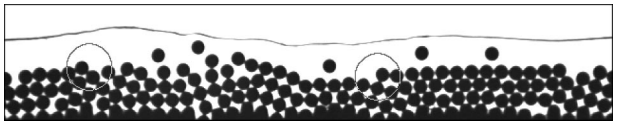

FIG. 17. A single image of the sequence at $t=2.0$ s. It shows a downward and an upward step which provoke the liftoff and the settling of beads respectively. Experiment D.

the range of $10\ \text{mm} < x < 40\ \text{mm}$ in the time period $0\ \text{s} < t < 3\ \text{s}$ and eight settling events in the range of $140\ \text{mm} < x < 170\ \text{mm}$ in the period $1.5\ \text{s} < t < 4\ \text{s}$. This basically resulted from bed structures, as shown in Fig. 17: A downward step in the bed forced the ejection of beads and an upward step made beads in saltation collide and come to rest. These structures were typically active for several seconds until the bed rearranged.

IV. CONCLUDING REMARKS

In this paper, the dynamics of particle transport in a turbulent water stream was investigated experimentally. We used an inclined channel in which the particle and water supplies at the inlet were controlled accurately and the movement of each particle was measured. This facility was intended to idealize the sediment transport in steep gravel-bed rivers. Consistently with field observations, preliminary experiments revealed substantial fluctuations in the measured solid discharge, whereas the flow conditions were kept stationary on average.

We ran a series of four experiments (A–D) with a growing number of processes involved, to understand and discriminate the origins of these fluctuations. Experiments provided clear evidence that these fluctuations resulted, to a large extent, from the finite size of the observation window. Experiments A and B done with a fixed bed showed that solid discharge also inherited stochastic properties exhibited by individual particles. Fluctuations were exacerbated when the bed was mobile (runs C and D); that is, deposition and entrainment of particles were made possible. Mobile bed experiments were also characterized by a spectacular change in particle transport behavior, notably in the occurrence of rolling and saltating regimes. Solid-discharge variations with time were intercorrelated to obtain a characteristic time of particle motion. For fixed bed experiments, the characteristic time was nothing but the average time for a particle to travel the length of the observation window. For mobile bed experiments, the characteristic times were found to be larger; it was mainly related to the mean downstream velocity of the saltating phase. A striking result is that, although the probability density function of the solid discharge differed significantly between runs C and D, there was not much difference between their intercorrelation functions. Another notable result is that solid discharge depended a great deal on bed arrangement. Although the solid discharge was kept constant for either experiment, the water discharge at equilibrium was 40% higher for experiment D than for experiment C; moreover, the saltating movement was more frequent for run D compared to run C. Regime transitions (rolling from rest, saltation from rolling) depended a great deal on the bed arrangement: It was shown that (i) the local dynamics (liftoff, settling) was largely dependent on the bed arrangement and (ii) there were space and time correlations in the regime transitions, implying collective changes in particle behavior. This observation is of fundamental importance from the theoretical viewpoint because it emphasizes the importance of taking into account particle arrangement in the study of regime transition. Apart from a few recent experimental investigations [16], there are very few theoretical or experimental works that have been devoted to this topic.

Compared to a usual laboratory channel used for sedimentation studies [15], our experimental setup differed by several characteristics. The main drawbacks were the small channel width and the particles, which were spherical and fairly monosized. They were necessary limitations that allowed us to capture the entire movement of a set of particles (on the order of 100 individuals). To our knowledge, this microstructural investigation has never been conducted previously and experiments helpfully supplement numerical simulations [17].

Further investigations are under way to study the particle movement under different flow conditions. For this purpose, a number of experiments have to be run by varying control parameters such as the solid and liquid discharges at the channel inlet as well as the channel slope.

ACKNOWLEDGMENTS

This study was supported by the Cemagref and funding was provided by "Programme Avenir" of Rhône Alpes Région, by the "Programme national risque naturels" of INSU/CNRS, by the "Programme national risque hydrologique" INSU/ECCO, and "Action Concertée Incitative Risques naturels" of the CNRS. We are grateful to the laboratory TSI (Nathalie Bochard, Jacques Jay, and Jean-Paul Schon).

APPENDIX

Using simple assumptions makes it possible to obtain the probability density function $P_{\dot{n}}$ of the flow rate $\dot{n}$. These assumptions are the following.

(i) The number of particles is distributed according to a Poisson distribution; that is, we have

$$P_N(N_i) = \frac{e^{-\mu}\mu^{N_i}}{N_i!},$$

where μ is the average number of particles contained in the observation window: $\mu = \mathbb{E}[N_i]$.

(ii) The particle velocity is Maxwellian; that is, its variations around the mean velocity are normally distributed:

$$P_u(u_i) = \frac{1}{\sqrt{2\pi}\sigma_u} \exp\left[-\frac{(u_i - \overline{u})^2}{2\sigma_u^2} \right],$$

where $\overline{u}$ is the mean velocity and σ_u^2 the velocity variance.

(iii) The velocity probability is independent of (i) the particle number as well as (ii) the velocity of close particles because flow is dilute.

We introduce $U=\Sigma_{i=1}^{N_i} u_i$ the sum of particle velocities (streamwise components) for the N_i particles included in the window. Since $\dot{n}=U/L$, the pdf P_U of U is related to that of $\dot{n}$ by $P_{\dot{n}}=LP_v(L\dot{n})$. Thus computing P_U is tantamount to computing $P_{\dot{n}}$. The probability P_U is obtained by summing the elementary probabilities of observing k particles whose velocity sum equals U—that is,

$$P_U = \sum_{k=1}^{\infty} \frac{e^{-\mu}\mu^k}{k!} P_k(U),$$

where P_k denotes the probability of observing the velocity sum (for k particles) equal to U:

$$P_k = \int_{-\infty}^{\infty} du_1 du_2 \cdots du_k P_u(u_1) P_u(u_2) \cdots P_u(u_k) \times \delta[U - (u_1 + u_2 + \cdots + u_k)],$$

$$P_k = \int_{-\infty}^{\infty} du_1 du_2 \cdots du_{k-1} P_u(u_1) P_u(u_2) \cdots P_u \times [U - (u_1 + u_2 + \cdots + u_{k-1})].$$

Taking the Fourier transform of P_k leads to

$$\mathcal{F}[P_k](\omega) = (\mathcal{F}[P_u](\omega))^k,$$

where $\mathcal{F}[P_k](\omega)=\int e^{i\omega U} P_k(U) dU$. The Fourier transform can be expanded into an infinite series:

$$\mathcal{F}[P_k](\omega) = \sum_{j=0}^{\infty} \frac{c_j^{(P_k)}}{j!} (i\omega)^n,$$

where $c_j^{(P_k)}=(-1)^j (d^j \ln \mathcal{F}[P_k]/d\omega^j)_{\omega=0}$ are called the cumulants. For a normal distribution, the two first cumulants correspond to the mean and variance while the cumulants of order larger than 2 are zero. Here we find that:

$$c_j^{(P_k)} = 2c_j^{(P_u)} \quad \text{for } j = 1,2,$$

$$c_j^{(P_k)} = 0 \quad \text{for } j \geqslant 3.$$

Finally we deduce that P_k is a normal distribution of mean $k\overline{u}$ and variance $k\sigma_u^2$: $P_k=\mathcal{N}[k\overline{u}, \sqrt{k}\sigma_u]$. One finally obtains

$$P_{\dot{n}} = \sum_{k=1}^{\infty} \frac{e^{-\mu}\mu^k}{k!\sqrt{2\pi k}} \frac{L}{\sigma_u} \exp\left[- \frac{(L\dot{n} - k\overline{u})^2}{2k\sigma_u^2} \right].$$

Expressing this result as

$$P_{\dot{n}} = \sum_{k=1}^{\infty} \frac{e^{-\mu}\mu^k}{k!} \mathcal{N}\left[\frac{k\overline{u}}{L}, \frac{\sqrt{k}\sigma_u}{L} \right],$$

it is straightforward to deduce the mean and variance of $P_{\dot{n}}$:

$$\mathbb{E}[P_{\dot{n}}] = \frac{\mu\overline{u}}{L},$$

$$\mathrm{Var}[P_{\dot{n}}] = \frac{\mu\sigma_u^2}{L^2}.$$

[1] P.-Y. Julien, *Erosion and Sedimentation* (Cambridge University Press, Cambridge, England, 1994).

[2] G. K. Batchelor, in *Theoretical and Applied Mechanics*, edited by P. Germain, J.-M. Piau, and D. Caillerie (Elsevier Science, Amsterdam, 1989), p. 27.

[3] P. Coussot and C. Ancey, Phys. Rev. E **59**, 4445 (1999).

[4] R. A. Bagnold, Proc. R. Soc. London, Ser. A **332**, 473 (1973).

[5] G. Seminara, L. Solari, and G. Parker, Water Resour. Res. **38**, 1249 (2002).

[6] N. J. Balmforth and A. Provenzale, in *Geomorphological Fluid Mechanics*, edited by N. J. Balmforth and A. Provenzale (Springer-Verlag, Berlin, 2001), p. 369.

[7] H. A. Einstein, *The bedload function for sediment transportation in open channel flow*, Technical Bulletin of the U.S. Department of Agriculture No. 1026 (U.S. GPO, Washington, D.C., 1950); see for an introduction W. H. Graf, *Hydraulics of Sediment Transport* (Water Resources Publications, Littleton, 1984).

[8] L. van Rijn, J. Hydraul. Eng. **110**, 1431 (1985).

[9] C. Ancey, F. Bigillon, P. Frey, J. Lanier, and R. Ducret, Phys. Rev. E **66**, 036306 (2002).

[10] C. Ancey, F. Bigillon, P. Frey, and R. Ducret, Phys. Rev. E **67**, 011303 (2003).

[11] *Disorder and Granular Media*, edited by D. Bideau and A. Hansen (North-Holland, Amsterdam, 1993).

[12] F. Rioual, Ph.D. thesis, University of Rennes I, 2002.

[13] G. E. Grant, Water Resour. Res. **33**, 349 (1997).

[14] D. Rickenmann, J. Hydraul. Eng. **117**, 1419 (1991).

[15] Y. Niño, M. Garcia, and L. Ayala, Water Resour. Res. **30**, 1907 (1994).

[16] A. N. Papanicolaou, S. P. Dipla, N. Evaggelopoulos, and S. Fotopoulos, J. Hydraul. Eng. **128**, 369 (2002); F.-C. Wu and Y.-J. Chou, *ibid.* **129**, 110 (2003).

[17] M. W. Scheeckle and J. M. Nelson, Sedimentology **50**, 279 (2003).